University of Glasgow

Kleckner, T.C. and Modotto, D. and Locatelli, A. and Mondia, J.P. and Linden, S. and Morandotti, R. and De Angelis, C. and Stanley, C.R. and van Driel, H.M. and Aitchison, J.S. (2005) Design, fabrication, and characterization of deep-etched waveguide gratings. *Lightwave Technology* 23(11):pp. 3832-3842.

http://eprints.gla.ac.uk/3981/

29th Febuary 2008

Glasgow ePrints Service
https://eprints.gla.ac.uk

Design, Fabrication, and Characterization of Deep-Etched Waveguide Gratings

Todd C. Kleckner, Daniele Modotto, *Member, IEEE*, Andrea Locatelli, Jessica P. Mondia, Stefan Linden, Roberto Morandotti, Costantino De Angelis, *Member, IEEE*, Colin R. Stanley, *Member, IEEE*, Henry M. van Driel, and J. Stewart Aitchison, *Senior Member, IEEE*

***Abstract*—One-dimensional (1-D) deep-etched gratings on a specially grown AlGaAs wafer were designed and fabricated. The gratings were fabricated using state-of-the-art electron beam lithography and high-aspect-ratio reactive ion etching (RIE) in order to achieve the required narrow deep air slots with good accuracy and reproducibility. Since remarkable etch depths (up to 1.5 μm), which completely cut through the waveguide core layer, have been attained, gratings composed of only five periods (and, thus, shorter than 6 μm) have a bandgap larger than 100 nm. A defect was introduced by increasing the width of the central semiconductor tooth to create microcavities that exhibit a narrow transmission peak (less than 7 nm) around the wavelength of 1530 nm. The transmission spectra between 1460 and 1580 nm have been systematically measured, and the losses have been estimated for a set of gratings, both with and without a defect, for different periods and air slot dimensions. Numerical results obtained via a bidirectional beam propagation code allowed the evaluation of transmissivity, reflectivity, and diffraction losses. By comparing experimental results with the authors' numerical findings, a clear picture of the role of the grating's geometric parameters in determining its spectral features and diffractive losses is illustrated.**

***Index Terms*—Defect waveguides, diffraction, gratings, photonic crystals, reflection, semiconductor waveguides.**

I. Introduction

PHOTONIC-CRYSTAL properties have been studied theoretically, and numerical simulations have been used to investigate the behavior of photonic-crystal-based components like waveguides, couplers, bends, and Y-junctions [1]. The proposed devices offer tantalizing opportunities for extremely compact optical integrated circuits [2], [3]. Both simulations and the first attempts at fabricating photonic-crystal components [4] have clearly indicated that strict control over the geometric parameters is required, as fabrication inaccuracies result in substrate and/or upper cladding scattering, which can considerably degrade the expected performance [5], [6].

One-dimensional (1-D) photonic crystals can be obtained by etching a grating into a ridge waveguide within a multilayer high-refractive-index substrate [7]. Light confinement is ensured in the vertical direction by the index contrast provided by the substrate layers, and in the horizontal direction by the etched ridge itself. The mode propagating along the ridge experiences the periodic variation of the dielectric properties, which gives rise to the band structure that governs device operation in both transmission and reflection.

More complex two-dimensional (2-D) photonic-crystal waveguide circuits are obtained from a regular lattice of cylindrical air holes etched in a high-refractive-index substrate or from a lattice of dielectric rods surrounded by air [1]. Waveguiding in the planar direction is achieved by perturbing the periodic lattice (for example, by removing a whole row of holes or rods), and vertical confinement is provided by the multilayer substrate. However, lithographic errors, incurred during the fabrication process, affect the realization of both 1-D and 2-D photonic-crystal devices [8], [9].

Krauss *et al.* report on the fabrication and testing of 1-D deep-etched gratings [7] and defect waveguides [10] conceived to work in a wavelength range between 820 and 930 nm, as mirrors and high-quality-factor microcavities, respectively. The periodic removal of the semiconductor provides a modulation of the refractive index larger than 2.2. The reported results were affected by diffraction losses and the defect peak maximum transmission varied between 6% and 18%. A simple transfer matrix routine, with a careful choice of the refractive indices, reproduced the transmission peak positions experimentally observed. Deep-etched gratings have found application as high-reflectivity compact mirrors in edge-emitting semiconductor lasers [11]–[13].

Alternatively, fabrication of shallow-etched gratings with etch depths insufficient to reach the waveguide core and their performance in both the linear and nonlinear regime are reported in [14] and [15]. The predicted refractive-index modulation is only 4.4×10^{-4}, and 4-mm-long gratings were required to produce a stopband. In these studies, the shallow etch helped to avoid the onset of radiation losses but resulted in a stopband narrower than 1 nm and, therefore, ineffective for broadband operation.

Manuscript received August 30, 2004; revised May 24, 2005. The work of T. C. Kleckner was supported by the Commonwealth Scholarship and Fellowship Plan and the NSERC Postgraduate Scholarship Program. The work of S. Linden was partially supported by the Alexander von Humboldt Foundation.

T. C. Kleckner was with the Department of Electronics and Electrical Engineering, University of Glasgow, Glasgow G12 8LT, U.K. He is now with the Lumerical Solutions, Inc., Vancouver, BC V6C 1H2, Canada.

D. Modotto, A. Locatelli, and C. De Angelis are with the Istituto Nazionale per la Fisica della Materia, Dipartimento di Elettronica per l'Automazione, Università di Brescia, Brescia 25123, Italy.

J. P. Mondia, S. Linden, and H. M. van Driel are with the Department of Physics, University of Toronto, Toronto ON M5S 1A7, Canada.

R. Morandotti is with the Institut National de la Recherche Scientifique, Université du Québec, Varennes, QC J3X 1S2, Canada.

C. R. Stanley is with the Department of Electronics and Electrical Engineering, University of Glasgow, Glasgow G12 8LT, U.K.

J. S. Aitchison is with the Edward S. Rogers, Sr. Department of Electrical and Computer Engineering, University of Toronto, Toronto, ON M5S 3G4, Canada.

Digital Object Identifier 10.1109/JLT.2005.857737

0733-8724/$20.00 © 2005 IEEE

In the following, experimental and numerical results on waveguide-based deep-etched gratings, which are amenable for the realization of grating-based mirrors and frequency agile filters, are reported. The structures were designed for the wavelength range between 1500 and 1560 nm, corresponding to the low-loss transmission window of optical fiber communication systems.

By systematically varying both the grating period and the dimensions of the semiconductor teeth, and by means of slight adjustments of the electron beam lithography process, the authors were able to fabricate sets of different devices exhibiting the stopband, the stopband edge, or the defect transmission peak in the wavelength range accessible with an $S + C$-band tunable laser.

A transmission matrix code and a more sophisticated bidirectional beam propagation method (BiBPM) [16]–[18] were used to design the grating parameters to achieve the desired transmission spectrum. The BiBPM takes one transverse dimension into account and is useful to analyze the field profile in close proximity to the grating. This knowledge can be subsequently used to understand the origin of losses through study of how the field emanates from the grating discontinuities. This numerical tool requires fewer computational resources than the commonly used finite-difference time-domain (FDTD) [19] code and permits a fast and systematic study of the grating performance.

II. Design and Fabrication

We fabricated deep-etched gratings on a multilayer $Al_xGa_{1-x}As$ wafer. We took advantage of existing knowledge on how to design the slab layers in order to minimize the diffraction losses, as widely discussed in the literature [7]–[9]. As the waveguide mode diffracts rapidly while travelling through the air slots within the grating, we tried to maximize the fraction of semiconductor within each grating period and keep the air regions much shorter than the diffraction length in air. This is an especially important design goal as significant overlap of the mode tails with either the upper/air or lower/substrate claddings results in huge diffraction losses [7]–[9]. Once the air slot thickness and the etch depth had been chosen, we designed a wafer with an extremely thin upper cladding and a narrow core in order to push the waveguide mode towards the wafer surface and to keep the mode tail away from the bottom of the air slots.

The resulting wafer design incorporates a 200-nm-thick $Al_{0.40}Ga_{0.60}As$ upper cladding, a 600-nm-thick $Al_{0.20}Ga_{0.80}As$ core, and a 4-μm-thick $Al_{0.40}Ga_{0.60}As$ lower cladding grown on a GaAs substrate. The wafer surface is capped by a 100-nm GaAs layer in order to prevent oxidation of the AlGaAs layers when exposed to air. This multilayer structure was grown by molecular beam epitaxy (MBE), and the resulting material exhibits low intrinsic losses in the wavelength range of interest [20].

Paying attention to what feature sizes are achievable with electron beam lithography, we selected a set of semiconductor teeth and air slot grating geometries that placed the band edge of the mirror-like grating close to 1530 nm and the transmission peak of the defect-state grating in the same wavelength range. For the purposes of design, we used Adachi's model [21] to calculate the refractive indices of the different wafer layers, and we used the effective refractive index of the unperturbed ridge waveguide for the refractive index of the semiconductor teeth.

Preliminary simulations with the transmission matrix routine indicate that a period in the range of 800–1100 nm and an air slot thickness between 150 and 300 nm are necessary to locate the band edge in the desired wavelength range. These geometric requirements, coupled with the need for large etch depths to minimize diffraction losses, necessitated fabrication with electron beam lithography and reactive ion etching (RIE).

Device fabrication began with the deposition of a 150-nm plasma-enhanced chemical vapor deposition (PECVD) silica etch mask layer upon which a 200-nm bilayer of polymethylmethacrylate (PMMA) was spun and irradiated with a 15-nm spot size 50-kV electron beam. Following development in a 2.5:1 solution of methyl-isobuthyl ketone (MIBK) developer and isopropyl alcohol, the pattern realized in PMMA was transferred to the underlying 150-nm silica etch mask through RIE in a CHF_3 plasma. After this pattern transfer process, residual PMMA was completely removed through low-power O_2 plasma cleaning to ensure a clean substrate, devoid of RIE grass resulting from microetch masking. Subsequent pattern transfer to the $Al_xGa_{1-x}As$ layers was obtained with a high-power RIE in a $SiCl_4$ chemistry to achieve the high-aspect-ratio gratings required [22]–[24]. Maximum etch depths for the 150-nm silica mask were realized through timed etches to calibrate the rate at which the etch mask was removed in the $SiCl_4$ chemistry. The resulting etch depths obtained were on the order of 1500 nm, corresponding to a 10:1 aspect ratio, given the smallest air slot dimensions of 150 nm. During the fabrication process, we observed that the dimensions of the patterned semiconductor teeth were very sensitive to the electron beam dose used during irradiation. The postexposure pattern dimensions as measured via high-resolution scanning electron microscope (SEM) images were cross-checked with the design dimensions to reveal that large variations in the exposure dose level can change the air slot width by as much as 80 nm for 1-μm grating periods.

Iterative device design, fabrication, testing, and redesign were performed to reconcile discrepancies between the measured transmissivity spectra and those predicted by the transmission matrix routine. In some cases, the magnitude of the shift of the band-edge position between experiment and theoretical prediction was on the order of hundreds of nanometers, where the defect was located outside the 120-nm tuning range of the external cavity laser used for the experiments. Previous work [7] and our measurements suggest that the effective refractive index of the semiconductor teeth is much lower than we predict based upon the effective index of the unperturbed waveguide mode. Agreement between experimental observations and simulations of the grating structure with the transmission matrix technique requires an assumed effective index of 3.152, in stark contrast to the value of 3.258 we predict using a mode solver and Adachi's refractive-index model for the AlGaAs alloys present in the wafer structure. As postulated by Krauss *et al.* [10], a thin oxidation layer upon the surfaces of the semiconductor teeth could result in a substantially smaller

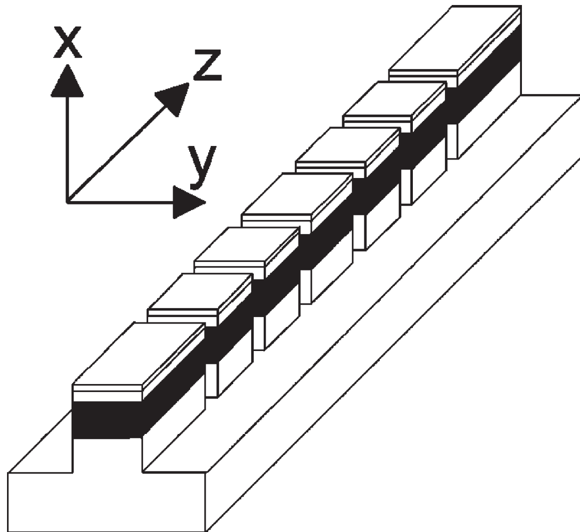

Fig. 1. Schematic 3-D drawing of the deep-etched grating (five-period grating, six air slots). The dark region is the core layer.

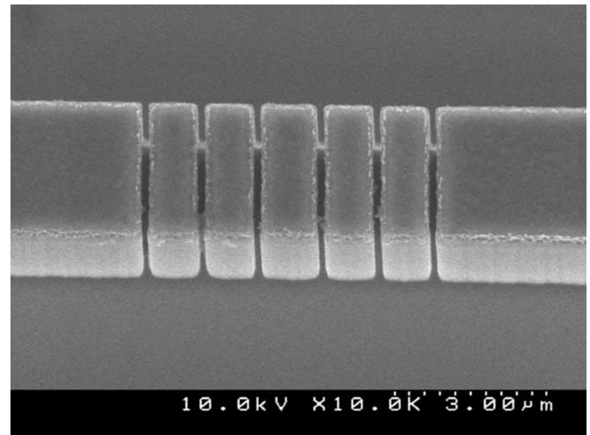

Fig. 2. SEM photograph of a five-period grating with defect. The six air slots go through the whole ridge height and the etch depth is 1.5 μm. The input and output waveguides are 2.5 μm wide and 1.5 mm long.

effective refractive index considering the refractive index of aluminum oxide is on the order of 1.6. In the following, we account for this difference by reducing the effective refractive index of the semiconductor teeth rather than introducing additional oxide surfaces as we do not precisely know either their thickness or their composition.

To produce gratings with parameters very close to the target geometry, we fabricated a host of devices with a series of slightly different electron beam doses. This allowed us to systematically increase the dimensions of the air slot while keeping the grating period constant. This variation in exposure conditions provides a mechanism by which very subtle and fine adjustments can be made to the devices during fabrication. Furthermore, this method allows for continuous variations in the grating geometry, instead of the discrete increments provided by the digital raster of the electron beam system.

A schematic drawing of the grating is displayed in Fig. 1 and an SEM photograph of one of the resulting devices is shown in Fig. 2; the input and output waveguides are 2.5 μm wide and the air slot depth is comparable to the ridge height ($\simeq$ 1.5 μm). Devices with both five and seven periods, corresponding to six and eight air slots, were fabricated and cleaved into structures with 1.5-mm-long waveguides on the input and output side.

III. Measurements

The light source used to measure the transmission spectrum was an external cavity laser tunable between 1460 and 1580 nm. The collimated laser output passed through a beam chopper and a polarizing beam-splitting cube, which rejects the transverse magnetic (TM) polarized light. The transmitted transverse electric (TE) polarized light was focused on the input waveguide facet by means of a 40× microscope objective, antireflection coated for operation around 1550 nm. The light at the output facet was collected through a second microscope objective and was directed onto the surface of a germanium photodetector. Proper alignment of the end-fire launch was ensured by imaging the waveguide output onto an infrared charge-coupled device (CCD) camera. The mode shape and waveguide throughput were optimized through adjustment of the relative position of the collimated beam, the input objective, and the sample. The emission wavelength of the computer-controlled laser could be varied across the 1460–1580 nm range in increments of 2.5 pm, and at each wavelength setting, the waveguide throughput was measured through lock-in detection of the signal on the photodiode.

TABLE I
Geometric Parameters of the Gratings

Device	d_{AlGaAs} (nm)	d_{AIR} (nm)	Δd_{AlGaAs} (nm)
M1	740	110	0
D1	825	120	120
D2	880	200	130
D3	790	280	170
D4	920	200	140

The measured transmissivity graphs exhibit closely spaced local maxima and minima due to the Fabry–Perot resonances of the cavity formed by the whole device (including input waveguide, grating, and output waveguide). The experimental setup was used to measure the Fabry–Perot fringes of identical waveguides (etch depth of 1.5 μm and ridge width of 2.5 μm) without the grating. These measurements were used to evaluate the losses of the ridge waveguides for a series of different lengths ranging between 1.5 and 3 mm. The measured losses, between 5 and 6 dB/cm, were caused by semiconductor intrinsic absorption and by scattering due to sidewall roughness.

We report results for five devices whose spectra have different feature dimensions. In Table I, we summarize the geometric dimensions of the considered fabricated gratings; d_{AlGaAs} is the semiconductor tooth thickness, d_{AIR} is the air slot thickness, and $\Delta d_{\mathrm{AlGaAs}}$ is the amount that the central semiconductor layer has been widened in order to create the defect state; the number of air slots is 6. These thicknesses have been estimated from SEM images.

Fig. 3 shows the measured transmissivity T for the "mirror-like" device M1 (five period/six air slot gratings) whose measured semiconductor tooth width and air slot width are

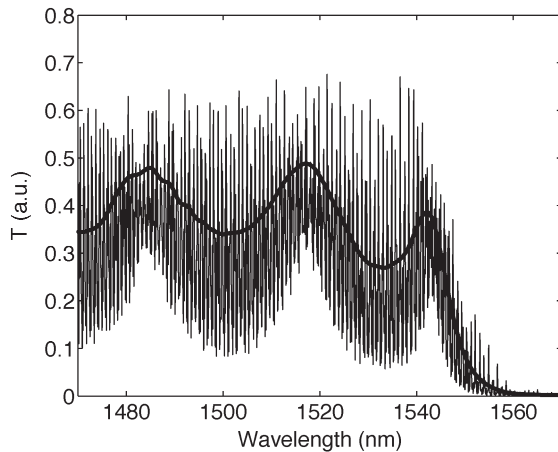

Fig. 3. Recorded transmission spectrum (narrow black line) and spectrum after the removal of high-frequency components (thick black line) for the mirror grating M1.

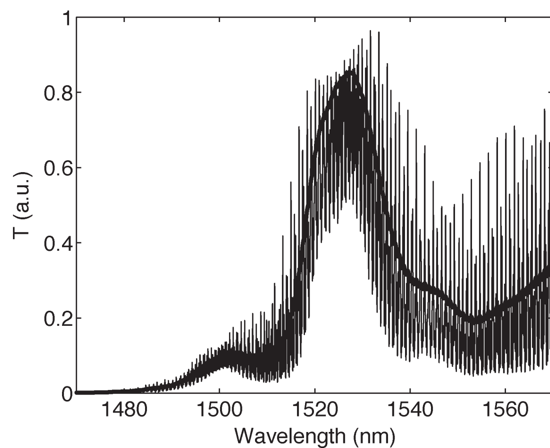

Fig. 4. Recorded transmission spectrum (narrow black line) and spectrum after removing the high-frequency oscillations (thick black line) for the grating with defect D1. The large peak FWHM is 14 nm, and it is located at 1527 nm.

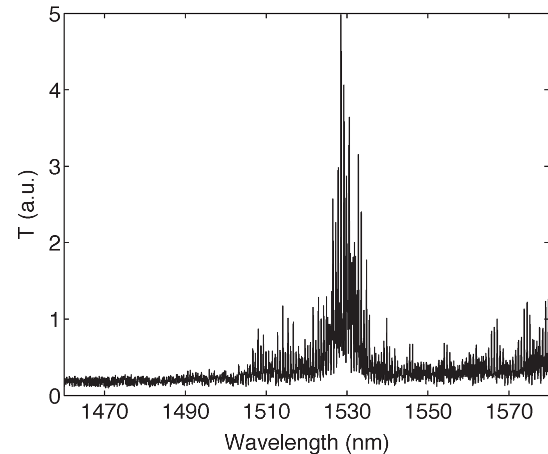

Fig. 5. Measured transmission spectrum (black line) for the grating with defect D2. The peak FWHM is 6 nm, and it is located at 1528 nm.

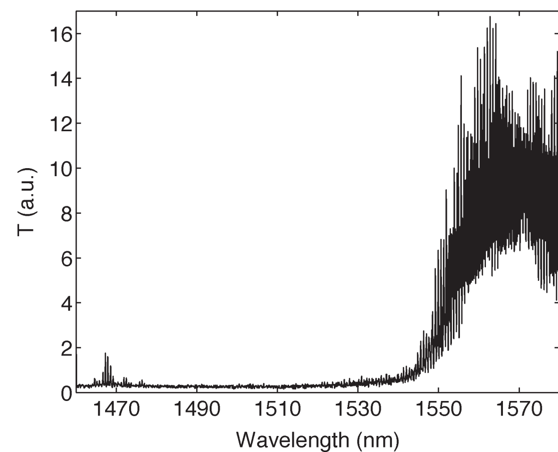

Fig. 6. Measured transmission spectrum (black line) for the grating with defect D3. Both the defect peak at 1467 nm and the broad band edge around 1560 nm can be recognized.

$d_{\mathrm{AlGaAs}} = 740$ nm and $d_{\mathrm{AIR}} = 110$ nm, respectively. The narrow black line, which is proportional to the photodetector output, was measured with a wavelength spacing of $\Delta\lambda = 0.1$ nm, and it is blurred by the Fabry–Perot fringes. The thick black line is obtained by removing the high-frequency components of the spectrum and normalizing the result to the measured maximum transmissivity. Thanks to the presence of the stopband, this device can be used as a high-reflectivity mirror for wavelengths longer than 1560 nm. Moreover, three transmission peaks are easily recognizable: 1) the first peak beside the stopband at 1543 nm; 2) the second-order transmission peak located around 1517 nm; and 3) a third peak around 1485 nm.

The spectrum of device D1 (which contains a grating with a defect) is shown in Fig. 4. The semiconductor and air slot thicknesses were designed assuming an effective refractive index of 3.34 and not taking into account the oxidation effects. As a result, the transmission peak introduced by the defect is not located inside our laser wavelength range of 1460–1580 nm. However, we note that a stopband exists for wavelengths shorter than 1490 nm, and the first-order transmission peak is located roughly at 1527 nm.

A defect transmission peak located in the middle of the stopband (at 1528 nm) is displayed in the spectrum of Fig. 5 referring to device D2. The transmission peak width appears to be on the order of 6 nm, but a precise evaluation is complicated as a result of the Fabry–Perot fringes.

In Fig. 6, we plot the transmissivity of the grating with defect D3. In this spectrum, a broad band edge is observed at 1560 nm, and the defect transmission peak is located at 1467 nm. Thus, the defect transmission peak and the first-order grating transmission peak are placed at the edges of the range accessible by the tunable laser source. By measuring the input and output power at the defect peak wavelength, we estimate that the transmissivity in the defect state is roughly 0.05.

The spectra reported in Figs. 5 and 6 were obtained from two devices whose nominal geometric parameters are the same, where the period is 1080 nm and the air slot width is 150 nm. Nevertheless, since the first device was exposed to the minimum electron beam dose and the second one to the maximum dose, this resulted in an appreciable change of the semiconductor tooth spacing and a consequent shift and deformation of the spectrum.

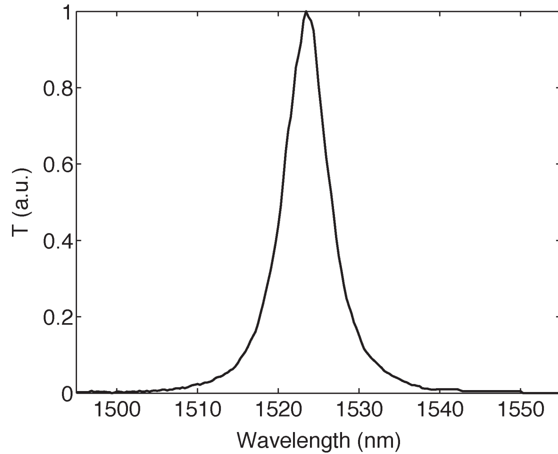

Fig. 7. Transmission spectrum measured using the monochromator and 250-fs-long pulses from the OPO for the grating with defect D4. The transmission peak is located at 1523 nm, and its FWHM is 7 nm.

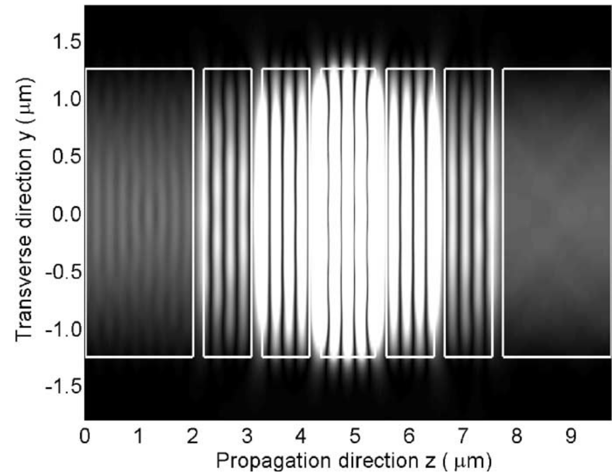

Fig. 8. Electric field in the segmented waveguide, obtained neglecting the vertical direction x of the real 3-D grating D2. The thin white lines display the borders between the semiconductor and air.

In order to more accurately determine the spectral width of the defect resonance, a tunable optical parametric oscillator (OPO) laser system was used to measure the transmissivity. The laser delivers 250-fs pulses, corresponding to a 20-nm spectral width, at a repetition rate of 77.8 MHz, tunable around 1530 nm. The defect transmissivity was measured by passing the output signal through a monochromator. The short pulse source allowed us to measure the transmission spectra without the presence of the Fabry–Perot resonances. The transmissivity of grating D4, measured with the OPO source, is reported in Fig. 7. The transmission peak is located at 1523 nm and its full-width at half-maximum (FWHM) is 7 nm.

IV. Comparison With Numerical Results

In this section, the main physical reasons underlying the observed performance are investigated. The low transmissivity measured in the defect waveguides is explored with an aim to identify more suitable choices for grating geometry and wafer design to realize higher throughput devices.

As illustrated in Fig. 6, the measured spectra of the defect gratings show that the defect transmission peak has an amplitude approximately ten times smaller than the transmissivity at the band edge. While the transmission matrix routine cannot account for diffraction as it does not include a description of the transverse dimensions, other numerical techniques are available. One numerical method that has been widely applied to accurately model high-refractive-index contrast structures is the FDTD technique [19]. As FDTD does not rely on any inherent approximations, it is well suited to study reflection and transmission phenomena at the grating interfaces [25], [26]. Despite the large memory requirements and computational burden, FDTD has been used to study corrugated waveguides [25] and deep-etched gratings [27].

Other means of calculation are based on a vectorial eigenmode expansion approach, which was efficiently implemented to model multilayer structures and deep-etched gratings [28]. In particular, it has been demonstrated that in order to minimize the diffraction losses, it would be preferable to have a low-refractive-index contrast between core and cladding, or rely on high contrast core–cladding interfaces to excite the propagation of Bloch modes, which would be lossless for a perfectly periodic structure devoid of manufacturing errors [8], [9].

Since we are studying a multilayer structure, the BiBPM is a suitable numerical tool with high accuracy and very short computational times [16]–[18]. By means of the scattering method formalism, the field continuity conditions are imposed at the air–semiconductor interfaces; the use of a wide angle propagator in each layer guarantees that even the portion of the field not propagating normally to the interfaces is correctly described. Moreover, the scattering formalism [16]–[18] avoids the rise of numerical instability. This method has already been successfully applied to the analysis of high index contrast segmented waveguides [18]. In our implementation, the presence of perfectly matched layers at the computational grid borders avoids the onset of spurious reflections coming back into the device region.

As a first example, we show the electric field in device D2: The semiconductor teeth are 880 nm wide, the central defect is 1010 nm wide, and each air slot is 200 nm wide. As we can include only one transverse dimension, we simulate the device twice; in the first simulation, we neglect the vertical transverse direction x, and in a second simulation, we neglect the horizontal transverse direction y (see Fig. 1). In order to choose the most appropriate effective refractive indices, we could start from the material indices and use the effective index method; nevertheless, our waveguide transverse dimensions are short compared to the wavelength and the variations in dielectric constant are large, and therefore, we do not assume *a priori* that the effective index reproduces the behavior of the three-dimensional (3-D) structure. Instead, we systematically modify the refractive indices used in the simulations to obtain agreement with the measured peak positions.

If we neglect the vertical transverse direction x, the grating device is modeled as a 2-D segmented waveguide (having air as cladding), and a semiconductor refractive index of 3.165 provides good agreement with experiments. The calculated electric field at the resonance wavelength of 1527 nm is displayed in

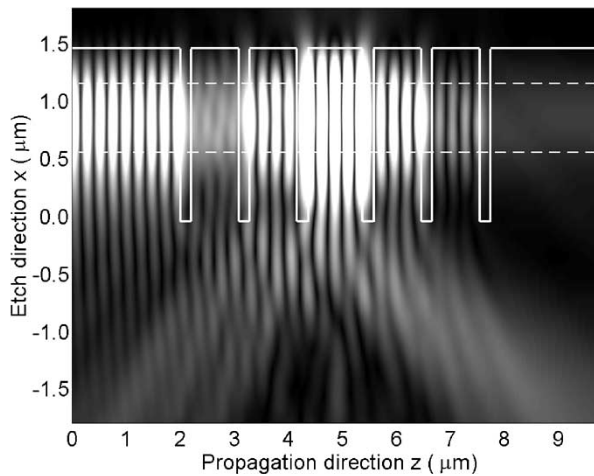

Fig. 9. Electric field in the periodically etched slab waveguide, obtained neglecting the horizontal transverse dimension y of the real 3-D grating D2. The thin white lines are the interfaces between the semiconductor and air; the dashed lines indicate the core layer of the wafer.

Fig. 8; the field is depicted on a linear grey scale where white represents the maximum field amplitude and black indicates the absence of field. We assume that this result is a good approximation of the field in the device seen from the top. The narrow straight white lines indicate the interfaces between air and semiconductor in the device. The structure operates as a cavity, and the electric field maxima in the central defect layer are easily recognized. It is worth noting that the field is well confined into the waveguide segments and the "mode" width does not change appreciably in the air slots. As such, we conclude that diffraction along the horizontal direction y should introduce negligible losses in the real 3-D device.

Fig. 9 shows the vertical profile of the electric field calculated by neglecting the horizontal direction y, but taking into account the vertical direction x, the grating is modeled like a 2-D etched slab waveguide. The field is displayed on a grey scale, and the solid lines indicate the borders between air and semiconductor, whereas the dashed lines indicate the 600-nm-thick core layer. The refractive index of the core layer is 3.215, and the refractive index of the upper and lower claddings is 3.115. When the etch depth is 1.5 μm, the resonance wavelength is 1523 nm. Actually, this picture shows the spatial distribution of the electric field in an infinite width ridge as seen from the side. The field seems well confined inside the core of the input and output waveguides, but when it passes through the grating region, a portion of the power radiates away into the lower substrate. Even if the device is operating at the resonance wavelength, the presence of a strong reflected field can be observed in the input section before the grating. A thorough analysis of Figs. 8 and 9 indicates that diffraction losses predominantly occur in the vertical direction, as would be expected from the narrower vertical versus horizontal "aperture" (i.e., the waveguide core) from which the radiation is emitted. We conclude that this diffractive mechanism is the main loss source in the manufactured devices.

Using the BiBPM, we calculated the transmission spectrum, the reflection spectrum, and the losses of D2. The transmissivity is the ratio between the power in the output waveguide mode

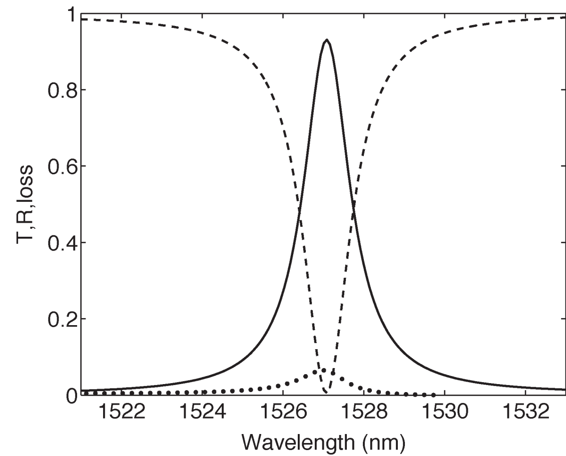

Fig. 10. Transmission T (continuous line), reflection R (dashed line), and loss (dotted line) of the segmented waveguide corresponding to D2.

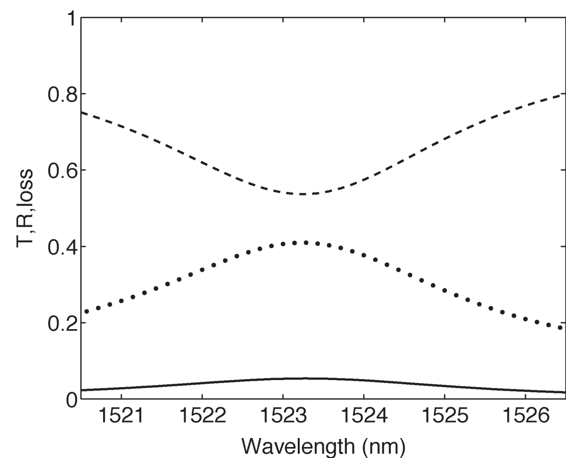

Fig. 11. Transmission T (continuous line), reflection R (dashed line), and loss (dotted line) of the periodically etched slab waveguide corresponding to D2.

and the power launched in the input waveguide, the reflection is the ratio between the power returning from the device and that launched into the input, and the losses are easily calculated from the energy balance. We perform the calculations for device D2 with 1.5-mm-long input and output waveguides to avoid near-field variations close to the deep-etched grating.

The spectra calculated by including the horizontal direction and the vertical direction are depicted in Figs. 10 and 11, respectively. The continuous line shows the transmissivity T, the dashed line shows the reflection R, and the dotted line displays the diffraction losses. These results confirm that diffraction takes place mainly in the vertical direction x and that a large fraction of the input power is reflected even if we are operating at the resonance wavelength. If we multiply the maximum transmissivity of the segmented waveguide by the maximum transmissivity of the etched slab, we obtain a defect peak transmissivity smaller than 10% of the band-edge transmissivity, and this value agrees with the measured peak amplitude (see Fig. 6).

The transmission peak in Fig. 11 is centered around 1523 nm and not at 1527 nm, because the etch depth of 1.5 μm does not completely remove the influence of AlGaAs at the slot

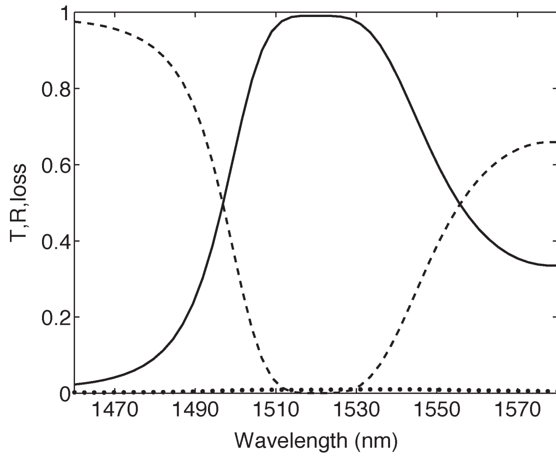

Fig. 12. Transmission T (continuous line), reflection R (dashed line), and loss (dotted line) of the segmented waveguide corresponding to D1.

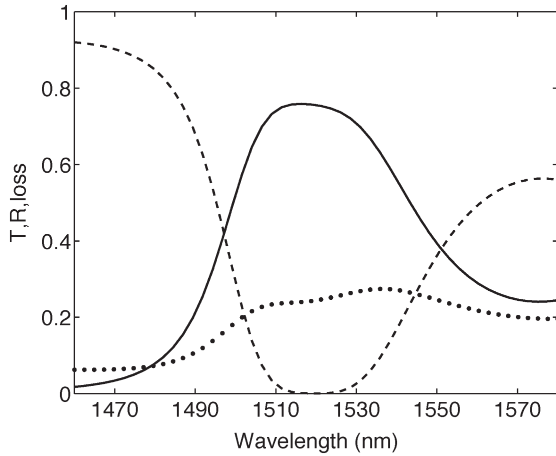

Fig. 13. Transmission T (continuous line), reflection R (dashed line), and loss (dotted line) of the periodically etched slab waveguide corresponding to D1.

bottoms; by fully etching the wafer, it is possible to position the transmission peak of the slab-based grating at 1527 nm.

The spectra for wavelengths around the band edge have been calculated via the BiBPM also for the device D1 ($d_{\mathrm{AlGaAs}} = 825$ nm and $d_{\mathrm{AIR}} = 120$ nm). The results of the top-view model are shown in Fig. 12, whereas the side-view results are depicted in Fig. 13. If we compare these results with the spectra for the defect device D2, we observe that the calculated transmission peak is much wider and the reflectivity at the resonance is only slightly larger than zero. Diffractive losses are largely present only in the vertical direction, but they never result in greater than 30% losses. These calculated spectra do not exhibit a perfect agreement with the experimental measurements of Fig. 4, but they do indicate the main broad peak centered around 1520 nm and a high-reflectivity region at wavelengths shorter than 1480 nm.

V. Role of the Grating Parameters

By systematically varying the wafer core thickness and the grating geometric parameters, we seek a better grating design. Furthermore, we aim to determine the sensitivity of the transmission spectra for variations in the fabricated devices.

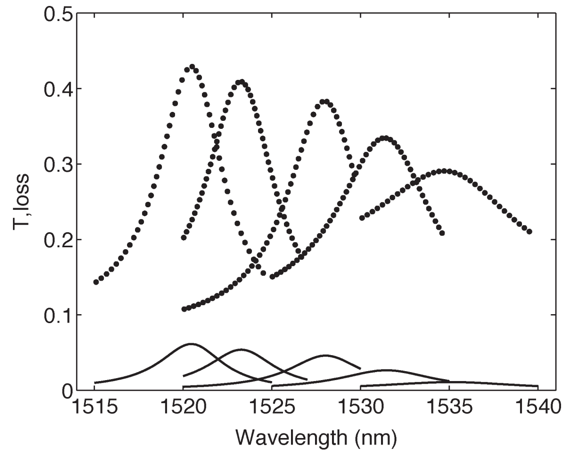

Fig. 14. Transmission T (continuous lines) and losses (dotted lines) versus wavelength λ for five different core thicknesses: 1) 500 nm; 2) 600 nm; 3) 700 nm; 4) 800 nm; and 5) 1000 nm (from left to right); the horizontal direction y has been neglected. The grating parameters d_{AlGaAs}, d_{AIR}, $\Delta d_{\mathrm{AlGaAs}}$ are those of D2, and the etch depth is 1.5 μm.

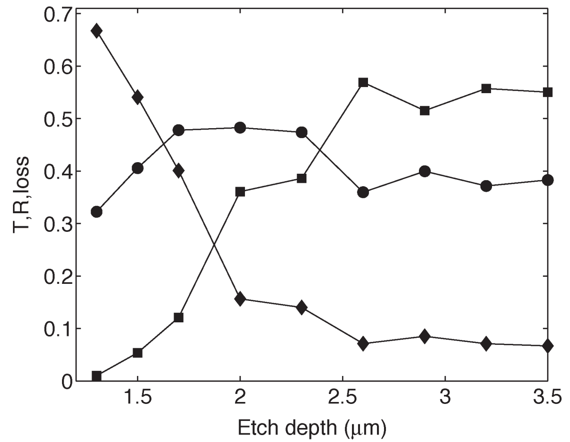

Fig. 15. Transmission T (squares), reflection R (diamonds), and losses (circles) as functions of the etch depth; the horizontal direction y has been neglected. The grating parameters d_{AlGaAs}, d_{AIR}, and $\Delta d_{\mathrm{AlGaAs}}$ correspond to D2.

We consider the grating with defect D2 where the core thickness is gradually changed, whereas the etch depth is fixed at 1500 nm. In Fig. 14, the transmissivity spectra and the losses, both calculated around the resonance wavelengths and neglecting the transverse direction y, are plotted as continuous and dotted lines, respectively. The five spectra refer to a core thickness of 500, 600, 700, 800, and 1000 nm (displayed from left to right). We observe that when the core becomes thicker, the transmissivity slightly decreases; on the other hand, a thinner core increases the losses, because the diffraction distance of the guided mode becomes shorter.

In the same defect device, we evaluated the influence of the etch depth. Intuition suggests that an air hole much deeper than the mode tails could prevent the onset of losses in the substrate. Our aim is to obtain an estimation of the minimum value of the etch depth to avoid the onset of strong reflections and diffraction losses. By increasing the etch depth of the defect grating D2, the transmissivity increases and the transmission peak wavelength shifts from 1523 nm towards 1527 nm. Fig. 15

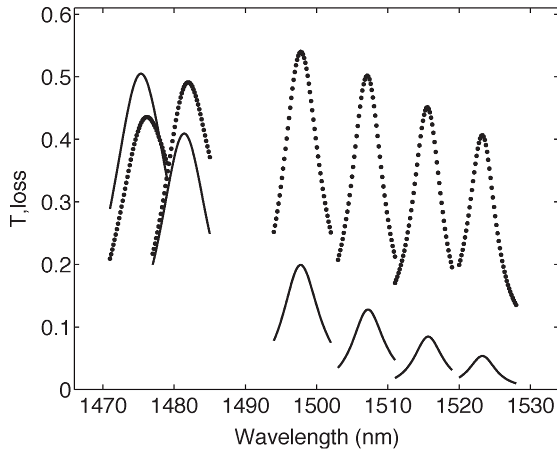

Fig. 16. Transmission T (continuous lines) and losses (dotted lines) for six different air slot thicknesses: 1) 100 nm; 2) 120 nm; 3) 140 nm; 4) 160 nm; 5) 180 nm; and 6) 200 nm (from left to right); the horizontal direction y has been neglected. The grating parameters are $d_{\mathrm{AlGaAs}} = 880$ nm and $\Delta d_{\mathrm{AlGaAs}} = 130$ nm (compare with the results for D2); the etch depth is 1.5 μm.

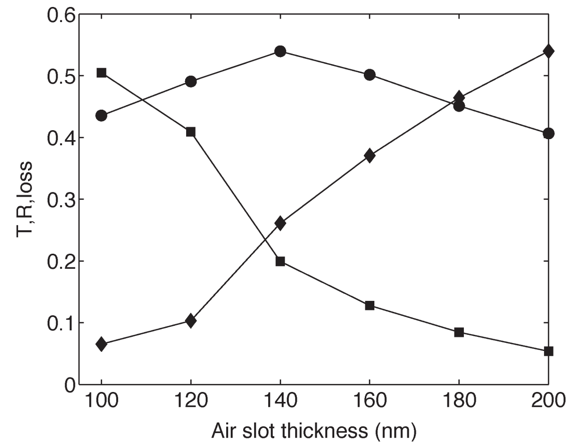

Fig. 18. Transmission T (squares), reflection R (diamonds), and losses (circles) as functions of the air slot thickness; the horizontal direction y has been neglected. The grating parameters are $d_{\mathrm{AlGaAs}} = 880$ nm and $\Delta d_{\mathrm{AlGaAs}} = 130$ nm (compare with the results for D2); the etch depth is 1.5 μm.

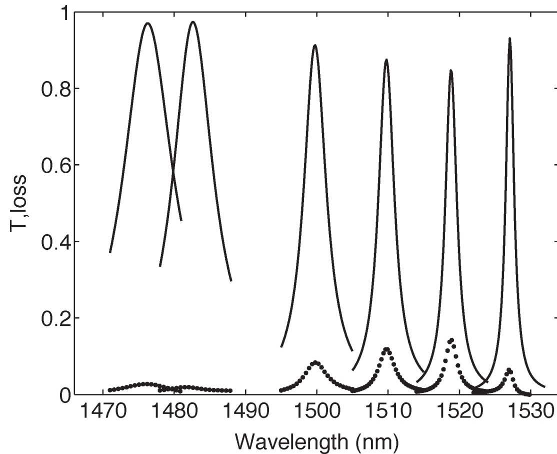

Fig. 17. Transmission T (continuous lines) and losses (dotted lines) for six different air slot thicknesses: 1) 100 nm; 2) 120 nm; 3) 140 nm; 4) 160 nm; 5) 180 nm; and 6) 200 nm (from left to right); the vertical transverse direction x has been neglected. The grating parameters are $d_{\mathrm{AlGaAs}} = 880$ nm and $\Delta d_{\mathrm{AlGaAs}} = 130$ nm (compare with the results for D2).

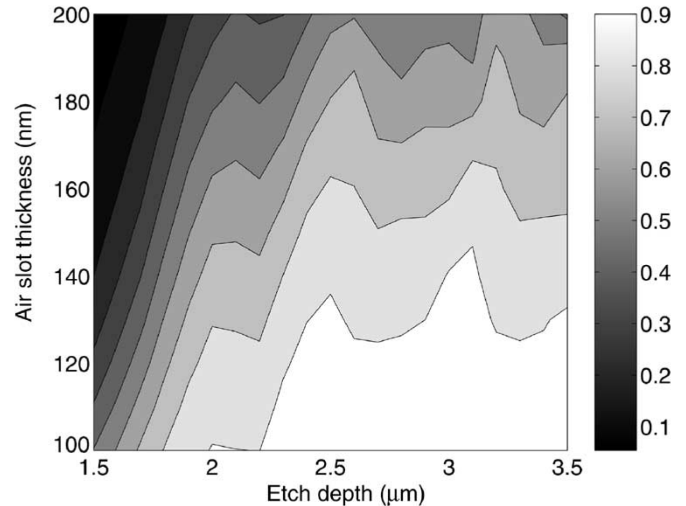

Fig. 19. Level curves in the etch depth/air slot thickness plane of the transmission T of the periodically etched slab corresponding to D2: $d_{\mathrm{AlGaAs}} = 880$ nm; $d_{\mathrm{AIR}} = 200$ nm; and $\Delta d_{\mathrm{AlGaAs}} = 130$ nm.

reports transmissivity, reflection, and losses at the resonance wavelength versus the etch depth; the core and air slot widths are held constant at 600 and 200 nm, respectively. When the bottom of the etched air slots overlaps with electric field (i.e., for an etch depth smaller than 1.7 μm), the transmissivity drops and the reflection is larger than 0.5. From the data of Fig. 15, we observe that diffraction couples always more than 30% of the injected mode power into the lower cladding.

In order to evaluate the role of the air slot thickness in determining the position and amplitude of the transmission peak and the diffraction losses, we calculated the spectra for $d_{\mathrm{AlGaAs}} = 880$ nm, $\Delta d_{\mathrm{AlGaAs}} = 130$ nm, and different values of the air slot width. Figs. 16 and 17 show the transmissivity and the losses, including the vertical and horizontal direction, respectively. We report results for air slot widths of 100, 120, 140, 160, 180, and 200 nm (grating D2), from left to right. The position of the peak shifts towards longer wavelengths as the air slot width increases, and the peak amplitude decreases. The side-view simulations (Fig. 16) are obtained for an etch depth of 1500 nm and indicate that the maximum transmissivity of the etched slab decreases from 0.5 to 0.05 when the air slot width is doubled from 100 nm to 200 nm, whereas its quality factor rises from $Q = 150$ to $Q = 400$. The diffraction losses predominantly occur in the vertical direction but for air slot widths greater than 160 nm, they become appreciable in the horizontal direction as well (see Fig. 17), proving that good device performance requires extremely small feature sizes.

Fig. 18 summarizes the results on transmission, reflection, and losses at the resonance wavelengths as functions of the air slot thickness. The maximum transmissivity wavelength moves from 1475 to 1523 nm when the air slot thickness is increased from 100 to 200 nm. For air slots wider than 180 nm, more than half of the power is reflected, whereas diffraction couples more

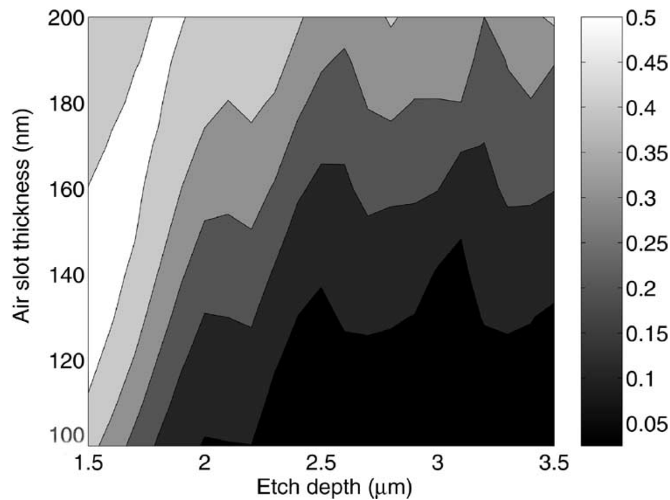

Fig. 20. Level curves in the etch depth/air slot thickness plane of the losses of the periodically etched slab corresponding to D2: $d_{\mathrm{AlGaAs}} = 880$ nm; $d_{\mathrm{AIR}} = 200$ nm; and $\Delta d_{\mathrm{AlGaAs}} = 130$ nm.

than 40% of the available power outside the guiding structure for each of the analyzed thicknesses.

Finally, we want to show how transmission and losses vary when both etch depth and slot thickness are changed; in fact, these two parameters can be controlled by the fabrication process and, thus, our analysis gives useful guidelines for the design of deep-etched gratings. The transmission at the resonance wavelength of the periodically etched slab corresponding to D2 is reported in Fig. 19 as a contour plot in the etch depth/air slot thickness plane. The data for an air slot width of 200 nm are also reported in Fig. 15, whereas the results for an etch depth of 1.5 μm are shown in Fig. 18; in fact, Figs. 15 and 18 can be obtained by slicing Fig. 19 along the planes $d_{\mathrm{AIR}} =$ 200 nm and etch depth $= 1.5$ μm, respectively. We observe that once the etch depth has been chosen, the transmission is a monotonically decreasing function of the slot thickness. On the other hand, if the slot width is given, the transmission becomes higher when the slot is deeper; nevertheless, the transmission is not a monotonic function of the etch depth, and there are small amplitude oscillations superimposed on the transmission trend. In brief, Fig. 19 clearly indicates that the maximum transmission can be close to 100% only for air slots deeper than 2 μm and narrower than 120 nm. In Fig. 20, we show the level lines of the losses in the etch depth/air slot thickness plane for the same periodically etched slab corresponding to D2. We observe that the losses are negligible for etch deeper than 2 μm and thin air slots; these diffraction losses exhibit the opposite behavior with respect to the transmission: They are a monotonically increasing function of the slot thickness and are remarkable for etch depths smaller than 2 μm. We have verified that the transmission is decreased by the onset of diffraction losses toward the substrate, and the back-reflection into the input waveguide can be larger than 20% only for air slots less deep than 2 μm.

The comparison between the top-view and side-view results shows that diffraction losses and back-reflection into the input waveguide act mainly in the vertical direction. We conclude that the transmissivity and reflectivity of the fabricated 3-D devices could be approximately calculated with the side-view model.

Good performance for waveguide-based deep-etched grating structures requires small air slots obtained through electron beam lithography. Coupled with the realization that maximizing transmissivity requires etch depths on the order of 2 μm, it follows that advanced RIE must complement electron beam lithography to realize next-generation commercial-quality devices.

VI. Conclusion

The authors report on the fabrication and testing of ridge waveguide-based deep-etched gratings fabricated in the AlGaAs–GaAs material system. It is confirmed that it is possible to realize high-reflectivity mirrors in the wavelength range of 1460–1580 nm, suitable for telecommunications applications. By introducing a wider semiconductor tooth in the grating, filters whose peak wavelength is centered between 1510 and 1530 nm were experimentally realized. Despite these accomplishments, the proposed filter cannot find application in its present form, because its performance is limited by severe reflection and diffraction losses. Exhaustive numerical modeling of the device, via a bidirectional propagation routine, indicated that the diffraction losses are due to radiation in the substrate and that the transmissivity can be maximized by increasing the etch depth and reducing the air slot thickness. These results agree with analyses reported in the literature and based on different numerical tools.

The present numerical study suggests that if the air slot aspect ratio is larger than 15, the transmissivity of the defect device becomes suitable for practical application. Even with state-of-the-art electron beam lithography coupled with reactive ion etching (RIE), it was not possible to realize such high-aspect-ratio air slots. Nevertheless, future technological advances will allow for the realization of compact gratings working as mirrors, filters, and microcavities in the near-infrared wavelength range and will enable new functionality to existing integrated optical platform technology.

Acknowledgment

The authors would like to thank the Natural Sciences and Engineering Research Council of Canada (NSERC), the Nortel Institute at the University of Toronto, and Photonics Research Ontario.

References

[1] J. D. Joannopoulos, R. D. Meade, and J. N. Winn, *Photonic Crystals, Molding the Flow of Light*. Princeton, NJ: Princeton Univ. Press, 1995.

[2] T. F. Krauss, R. M. De La Rue, and S. Brand, “Two-dimensional photonic-bandgap structures operating at near-infrared wavelengths,” *Nature*, vol. 383, no. 6602, pp. 699–702, Oct. 1996.

[3] T. F. Krauss and R. M. De La Rue, “Photonic crystals in the optical regime—Past, present and future,” *Prog. Quantum Electron.*, vol. 23, no. 2, pp. 51–96, Mar. 1999.

[4] S. Y. Lin, E. Chow, S. G. Johnson, and J. D. Joannopoulos, “Demonstration of highly efficient waveguiding in a photonic crystal slab at the 1.5 μm wavelength,” *Opt. Lett.*, vol. 25, no. 17, pp. 1297–1299, Sep. 2000.

[5] H. Benisty, C. Weisbuch, D. Labilloy, M. Rattier, C. J. M. Smith, T. F. Krauss, R. M. De La Rue, R. Houdré, U. Oesterle, C. Jouanin, and D. Cassagne, “Optical and confinement properties of two dimensional photonic crystals,” *J. Lightw. Technol.*, vol. 17, no. 11, pp. 2063–2077, Nov. 1999.

[6] H. Benisty, D. Labilloy, C. Weisbuch, C. J. M. Smith, T. F. Krauss, D. Cassagne, A. Beraud, and C. Jouanin, "Radiation losses of waveguide-based two-dimensional photonic crystals: Positive role of the substrate," *Appl. Phys. Lett.*, vol. 76, no. 5, pp. 532–534, Jan. 2000.

[7] T. F. Krauss and R. M. De La Rue, "Optical characterization of waveguide based photonic microstructures," *Appl. Phys. Lett.*, vol. 68, no. 12, pp. 1613–1615, Mar. 1996.

[8] W. Bogaerts, P. Bienstman, D. Taillaert, R. Baets, and D. De Zutter, "Out-of-plane scattering in photonic crystal slabs," *IEEE Photon. Technol. Lett.*, vol. 13, no. 6, pp. 565–567, Jun. 2001.

[9] ——, "Out-of-plane scattering in 1-D photonic crystal slabs," *Opt. Quantum Electron.*, vol. 34, no. 1–3, pp. 195–203, Jan.–Mar. 2002.

[10] T. F. Krauss, B. Vögele, C. R. Stanley, and R. M. De La Rue, "Waveguide microcavity based on photonic microstructures," *IEEE Photon. Technol. Lett.*, vol. 9, no. 2, pp. 176–178, Feb. 1997.

[11] T. F. Krauss, O. Painter, A. Scherer, J. S. Roberts, and R. M. De La Rue, "Photonic microstructures as laser mirrors," *Opt. Eng.*, vol. 37, no. 4, pp. 1143–1148, Apr. 1998.

[12] L. Raffaele, R. M. De La Rue, J. S. Roberts, and T. F. Krauss, "Edge-emitting semiconductor microlasers with ultrashort-cavity and dry-etched high-reflectivity photonic microstructure mirrors," *IEEE Photon. Technol. Lett.*, vol. 13, no. 3, pp. 176–178, Mar. 2001.

[13] L. Raffaele, R. M. De La Rue, and T. F. Krauss, "Ultrashort in-plane semiconductor microlasers with high-reflectivity microstructured mirrors," *Opt. Quantum Electron.*, vol. 34, no. 1–3, pp. 101–111, Jan.–Mar. 2002.

[14] P. Millar, R. M. De La Rue, T. F. Krauss, J. S. Aitchison, N. G. R. Broderick, and D. J. Richardson, "Nonlinear propagation effects in an AlGaAs Bragg grating filter," *Opt. Lett.*, vol. 24, no. 10, pp. 685–687, May 1999.

[15] N. G. R. Broderick, P. Millar, D. J. Richardson, J. S. Aitchison, R. M. De La Rue, and T. F. Krauss, "Spectral features associated with nonlinear pulse compression in Bragg gratings," *Opt. Lett.*, vol. 25, no. 10, pp. 740–742, May 2000.

[16] P. L. Ho and Y. Y. Lu, "A stable bidirectional propagation method based on scattering operators," *IEEE Photon. Technol. Lett.*, vol. 13, no. 12, pp. 1316–1318, Dec. 2001.

[17] ——, "A bidirectional beam propagation method for periodic waveguides," *IEEE Photon. Technol. Lett.*, vol. 14, no. 3, pp. 325–327, Mar. 2002.

[18] A. Locatelli, D. Modotto, C. De Angelis, F. M. Pigozzo, and A. D. Capobianco, "Nonlinear bidirectional beam propagation method based on scattering operators for periodic microstructured waveguides," *J. Opt. Soc. Amer., B, Opt. Phys.*, vol. 20, no. 8, pp. 1724–1731, Aug. 2003.

[19] A. Taflove and S. C. Hagness, *Computational Electrodynamics: The Finite-Difference Time-Domain Method*. Norwood, MA: Artech House, 2000.

[20] J. S. Aitchison, D. C. Hutchings, J. U. Kang, G. I. Stegeman, and A. Villeneuve, "The nonlinear optical properties of AlGaAs at the half band gap," *IEEE J. Quantum Electron.*, vol. 33, no. 3, pp. 341–348, Mar. 1997.

[21] S. Adachi, "GaAs, AlAs and $Al_xGa_{1-x}As$: Material parameters for use in research and device applications," *J. Appl. Phys.*, vol. 58, no. 3, pp. R1–R29, Aug. 1985.

[22] T. F. Krauss, Y. P. Song, S. Thoms, C. D. W. Wilkinson, and R. M. De La Rue, "Fabrication of 2-D photonic bandgap structures in GaAs/AlGaAs," *Electron. Lett.*, vol. 30, no. 17, pp. 1444–1446, Aug. 1994.

[23] P. Millar, R. Harkins, and J. S. Aitchison, "Fabrication of low loss, waveguide grating filters using electron beam lithography," *Electron. Lett.*, vol. 33, no. 12, pp. 1031–1032, Jun. 1997.

[24] C. J. M. Smith, S. K. Murad, T. F. Krauss, R. M. De La Rue, and C. D. W. Wilkinson, "Use of polymethylmethacrylate as an initial pattern transfer layer in fluorine- and chlorine-based reactive-ion etching," *J. Vac. Sci. Technol. B*, vol. 17, no. 1, pp. 113–117, Jan. 1999.

[25] R. W. Ziolkowski and J. B. Judkins, "Nonlinear finite-difference time-domain modeling of linear and nonlinear corrugated waveguides," *J. Opt. Soc. Amer., B, Opt. Phys.*, vol. 11, no. 9, pp. 1565–1575, Sep. 1994.

[26] R. Scarmozzino, A. Gopinath, R. Pregla, and S. Helfert, "Numerical techniques for modeling guided-wave photonic devices," *IEEE J. Sel. Topics Quantum Electron.*, vol. 6, no. 1, pp. 150–162, Jan.–Feb. 2000.

[27] R. Jambunathan and J. Singh, "Design studies for distributed Bragg reflectors for short-cavity edge-emitting lasers," *IEEE J. Quantum Electron.*, vol. 33, no. 7, pp. 1180–1189, Jul. 1997.

[28] P. Bienstman and R. Baets, "Optical modelling of photonic crystals and VCSELs using eigenmode expansion and perfectly matched layers," *Opt. Quantum Electron.*, vol. 33, no. 4–5, pp. 327–341, Apr.–May 2001.

Todd C. Kleckner received the B.Sc. degree in engineering physics, with distinction, from the University of Alberta, Edmonton, AB, Canada, in 1996, and the M.A.Sc. degree in electrical engineering from the University of British Columbia, Vancouver, BC, Canada, in 1998, for research on thermal modeling of advanced heterostructure devices. His Ph.D. studies, undertaken at the Department of Electronics and Electrical Engineering, University of Glasgow, Glasgow, U.K., from 1998 to 2001, assessed the feasibility of periodically disordered superlattice waveguides for optical frequency conversion.

From 2001 until 2003, he was an R&D Scientist with Galian Photonics Inc., Vancouver. Since that time, he cofounded Lumerical Solutions, Inc., Vancouver, an emerging computational modeling company focused on providing design solutions for next-generation optical devices.

Daniele Modotto (M'04–A'04–M'04) received the Laurea degree (*cum laude*) in electronic engineering and the Ph.D. degree in telecommunications from the University of Padova, Padova, Italy, in 1996 and 2000, respectively.

From 2000 to 2001, he was with the Department of Electronics and Electrical Engineering, University of Glasgow, Glasgow, U.K., where he was involved in nonlinear wavelength conversion modeling. Since November 2001, he has been working at the University of Brescia, Brescia, Italy. His research interests are nonlinear optics and passive waveguide components for telecommunications.

Andrea Locatelli was born in Seriate, Bergamo, Italy, in 1977. He received the Laurea degree (*cum laude*) in electronic engineering and the Ph.D. in information engineering from the University of Brescia, Brescia, Italy, in 2001 and 2004, respectively.

His main research interests include nonlinear optics and numerical modeling of waveguide components for telecommunications.

Jessica P. Mondia received the B.Sc. degree in physics (with honors) from the University of Victoria, Victoria, BC, Canada, in 1996, the M.Sc. degree in physics from the University of Toronto, Toronto, ON, Canada, in 1998, where she focused on two-photon absorption in low-temperature GaAs, and the Ph.D. degree from the University of Toronto.

She is currently working at the Optics, Information, and Photonics Max-Planck Group, University of Erlangen-Nuremberg, Erlangen, Germany.

Stefan Linden received the diploma in physics with distinction from the University in Karlsruhe, Karlsruhe, Germany, in 1998. During his Ph.D. studies at the Max-Planck-Institut für Festkörperforschung, Stuttgart, Germany, from 1998 to 2002, he worked on the optical properties of periodically arranged gold nanoparticles.

Afterwards, he spent a year in the group of Prof. H. van Driel at the University of Toronto with a Feodor Lynen Research Fellowship from the Alexander von Humboldt Foundation. Since 2003, he has been with the Institut für Nanotechnologie at the Forschungszentrum Karlsruhe in der Helmholtz-Gemeinschaft, Germany.

Roberto Morandotti received the M.Sc. degree in experimental nuclear physics from the University of Genova, Genova, Italy, in 1993. From February 1996 to December 1998, he worked toward the Ph.D. degree at the University of Glasgow, Glasgow, U.K., where his research activity focused on the study of the linear and nonlinear properties of optical discrete systems.

After spending one year in Glasgow as a Research Assistant, he moved to the Weizmann Institute of Science, Rehovot, Israel, and, finally, to the University of Toronto, Toronto, ON, Canada, to work on the characterization of novel optical structures. Since June 2003, he has been an Associate Professor in the "Ultrafast Optical Processing" group, recently established at INRS-EMT, University of Quebec, Montreal, QC, Canada. His research interests mainly deal with the linear and nonlinear properties of periodic structures, both in III–V semiconductors and silica.

Costantino De Angelis (M'04–A'04–M'04) was born in Padova, Italy, in 1964. He received the Laurea degree (*cum laude*) in electronic engineering and the Ph.D. degree in telecommunications from the University of Padova, Padova, Italy, in 1989 and 1993, respectively.

From 1993 to 1994, he was with the Department of Mathematics and Statistics, University of New Mexico, Albuquerque, NM. From 1995 to 1997, he was Assistant Professor at the Department of Electronics and Informatics of the University of Padova. From 1997 to 1998, he was with the Institut de Recherche en Communications Optiques et Microondes (IRCOM) at the University of Limoges, Limoges, France. Since 1998, he has been a Professor of electromagnetic fields at the University of Brescia, Brescia, Italy. His fields of technical interest are optical communications, soliton propagation, and photonics. He has authored or coauthored about 120 papers and conference contributions.

Colin R. Stanley (M'01) joined the Department of Electronics and Electrical Engineering at the University of Glasgow, U.K., in 1972 as a Research Fellow, and was subsequently appointed Lecturer (1974), Senior Lecturer (1982), Reader (1989), and Personal Professor (1992). He was responsible for establishing the Glasgow research activity into the molecular beam epitaxy (MBE) of III–V semiconductors in 1977 and since then has been author or coauthor of over 200 papers and conference presentations on MBE and related topics. He spent six months from October 1997 on industrial secondment with Motorola in East Kilbride under a scheme financed by the Royal Academy of Engineering.

Prof. Stanley is a Member of the IEE.

Henry M. van Driel was born in Breda, Netherlands. He received the B.Sc. and Ph.D. degrees from the University of Toronto, Toronto, ON, Canada, in 1970 and 1975, respectively.

Following postdoctoral work at the University of Arizona, Tucson, he assumed an academic appointment at the University of Toronto, where he is presently Professor of Physics. He was a Visiting Scientist at Harvard University, the University of Amsterdam, the Netherlands, and the Max Planck Institute für Festkörperforschung, Stuggart, Germany. He is the author of more than 230 papers in the field of ultrashort pulse laser physics and the interaction of optical pulses with semiconductors.

Prof. van Driel is a Fellow of the American Physical Society and the Royal Society of Canada.

J. Stewart Aitchison (M'96–SM'00) received the B.Sc. degree, with first class honors, and the Ph.D. degree from the Physics Department, Heriot-Watt University, Edinburgh, U.K., in 1984 and 1987, respectively. His dissertation research was on optical bistability in semiconductor waveguides.

From 1988 to 1990, he was a Postdoctoral Member of Technical Staff at Bellcore, Red Bank, NJ. His research interests were in high nonlinearity glasses and spatial optical solitons. He joined the Department of Electronics and Electrical Engineering, University of Glasgow, U.K., in 1990 and was promoted to a personal chair as Professor of Photonics in 1999. His research was focused on the use of the half bandgap nonlinearity of III–V semiconductors for the realization of all-optical switching devices and the study of spatial soliton effects. He also worked on the development of quasi-phase matching techniques in III–V semiconductors, monolithic integration, optical rectification, and planar silica technology. His research group developed novel optical biosensors, waveguide lasers, and photosensitive direct writing processes based around the use of flame hydrolysis deposited (FHD) silica. In 1996, he was the holder of a Royal Society of Edinburgh Personal Fellowship and carried out research on spatial solitons as a Visiting Researcher at CREOL, University of Central Florida, Orlando. He currently holds the Nortel Institute Chair in Emerging Technology at the University of Toronto, Toronto, ON, Canada. His research interests cover all-optical switching and signal processing, optoelectronic integration, and optical biosensors. His research has resulted in seven patents, around 130 journal publications, and 200 conference publications.

Dr. Aitchison is a Member of the Optical Society of America and a Fellow of the Institute of Physics London.